MICROWAVE RADIOMETRY IMAGING FOR FOREST FIRE DETECTION: A SIMULATION STUDY

S. Bonafoni, F. Alimenti, G. Angelucci, and G. Tasselli

Department of Electronic and Information Engineering (DIEI)
University of Perugia, via G. Duranti 93, Perugia 06125, Italy

Abstract—This paper deals with passive microwave imaging for fire detection by means of a single-channel ground-based radiometer. The simulation of images sensed in the presence of fire spots under different environmental and operative conditions will be presented. We will refer to a low-cost ground-based radiometer operating at 12.65 GHz. Scenarios where fires are un-visible and IR sensors are not useful with respect to a microwave imager will be investigated in deep, such as in the presence of vegetation canopy optically masking fire sources and smoke plumes in the early stage. These simulations will assess limits and capabilities of microwave imaging for the identification of little fires masked by forest areas.

1. INTRODUCTION

In each summer thousands of square kilometers are burned out by forest fires with a great damage for the environment, structures and persons. Fires are also serious threat inside private and public buildings, industrial or storage areas, railway and metro stations. The fire statistics provided by Fire Service Academy (Netherlands Institute for Safety) report an average of 20.7 annual fatalities per million inhabitants occurred in the European Union (data of the year 2008).

Currently active fire monitoring and fire danger potential detection are provided by satellite-based infrared (IR) sensors, using well assessed algorithms [1]. From space, fires in the early stage masked by vegetation are not detectable, this because they are too small and can easily be confused with other sources of human and natural origin.

Concerning ground-based systems, fire detection is an operational challenge usually faced with both IR and optical sensors. High-resolution IR cameras are able to detect small fires from great distances, while optical sensors (visual cameras) primarily detect the smoke plume due to the fire. However, the variation of illumination conditions and the variety of backgrounds negatively influence the detection mechanisms. In particular, IR and optical instruments fail in the presence of obstacles optically masking the fire source. To overcome this shortcoming, the approach with the microwave radiometry seems to be promising [2–4], even if we have to cope with a worse spatial resolution. Microwaves can penetrate vegetation layers detecting a target even if it is optically masked to an external observer, and lower frequencies seem to be better suited to look through the forest vegetation. However, the issue of a larger antenna footprint on fire spot detection has to be addressed, relating possible false alarms to spatial resolution, noise instrumentation and scenario characteristics. Here it is important to note that false alarms occur also with a pure IR technology in the absence of obstacles (sun reflections by rocks and water, etc.). To solve this problem a combination of IR and microwave imaging can be used. With such an approach one can take advantage from both the high spatial resolution of IR and the obstacle penetrating capability of microwaves.

In this work, the remote sensing of fire spots by a ground-based single-channel microwave radiometer is treated.

While actual single-spot fire measurements by a microwave radiometer are promising under different conditions and in particular in presence of obstacles [5, 6], in order to make the radiometric system useful in practical situations a microwave image of the observed scene has to be constructed [7].

Such an image will be useful to identify the location of the hottest points by a mechanically or electronically scanning antenna. From open literature, actual or simulated imaging of environmental scenarios in presence of fire by a ground-based microwave radiometer, especially fires in the early stage covered by a dense vegetation canopy, are not yet available.

The aim of this work is to illustrate the imaging of a scanning microwave radiometer and to simulate the images sensed in presence of fire spots under different conditions. We will refer to the low-cost microwave radiometer operating at 12.65 GHz and developed for this purposes in [5, 6].

Therefore, these simulations will assess the identification capability of little fires by means of microwave radiometry, exploring different environmental and operative conditions. However, we will

investigate in deep scenarios with fires where visible and IR sensors are not useful and performing with respect to a microwave imager, i.e., in the presence of vegetation canopy optically masking the fire source and the smoke plume in the early stage.

With respect to fire detection by microwaves, different questions arise. The first one is related to the maximum range that can be achieved in actual situations, taking into account the antenna beam and the related spatial resolution. Another question is associated with the identification of scenarios minimizing false alarms once established the radiometer technical and geometrical characteristics.

2. SCAN GEOMETRY CONSIDERATIONS

The proposed radiometric imaging is performed with the antenna beam of a ground-based single-channel microwave radiometer, based at height h, covering the target area by a suitable motion of the scanning mechanism. A first requirement for the resulting antenna footprint is to move in the swath avoiding or not overlaps during the scan, depending on application, selecting a proper sampling frequency and integration time. The measurement provided by a microwave radiometer is the antenna temperature T_A, which is the observed brightness temperature $T_B(\theta, \varphi)$ distribution of the sensed scenario convolved with the antenna
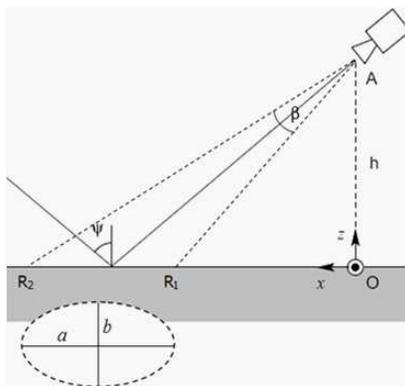

Figure 1. Scene detected by microwave radiometer. A antenna; h height of the antenna from ground; ψ incidence angle; β antenna half-power beam width; R_1 and R_2 minimum and maximum distance between footprint and origin. The dashed ellipse, with a and b major and minor radius, is the antenna footprint of the half-power beam width in the x-y plane.

power pattern $F(\theta, \varphi)$ [8]:

$$T_A = \frac{\iint_{4\pi} T_B(\theta, \varphi) F(\theta, \varphi) d\Omega}{\iint_{4\pi} F(\theta, \varphi) d\Omega} \tag{1}$$

where θ is the elevation angle, φ is the azimuth angle, $d\Omega = \sin \theta d\theta d\varphi$ is the elemental solid angle. The scan geometry is shown in Fig. 1, where the coordinate system is fixed to the ground: the antenna coordinates are $(0, 0, h)$ and the sensed area lies in the x-y plane.

Since $T_B(\theta, \varphi)$ gives the terrain brightness temperature values for any (θ, φ) at the current beam position, the $(\theta, \varphi) \leftrightarrow (x, y)$ correspondence is conveniently derived as in [9].

In the following two sub-sections, we will illustrate two scanning methods, namely the conical and the linear, highlighting pro and con.

2.1. Conical Scanning

Since the T_B of the target depends, in addition to frequency and polarization, on the incidence angle ψ, in the conical scanning each pixel in a single sweep (or scan) is observed at the same ψ [9, 10]. To produce an image of the scenario, we have to change the value of ψ at each sweep.

An example of antenna footprints for an image sensed in a conical mode by a microwave radiometer with an antenna half-power beam width $\beta = 6°$ and based at $h = 3\,\mathrm{m}$ is illustrated in Fig. 2. In this simulation, the sweeping or scan angle (γ_{sw}) is 120° and the incidence angle ψ ranges from 68° to 20°. Also, overlaps are avoided during the scan.
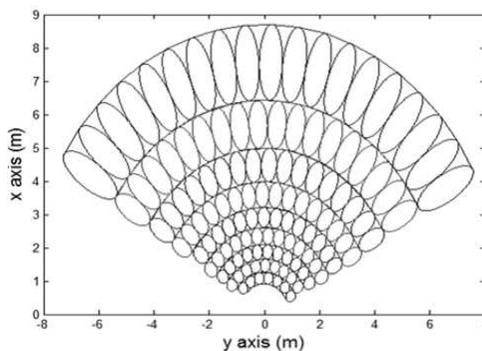

Figure 2. Conical scanning: antenna footprints of the half-power beam width plotted in an image sensed by a microwave radiometer with $\beta = 6°$ and based at $h = 3\,\mathrm{m}$. The sweeping angle γ_{sw} is 120° and the incidence angle ψ ranges from 68° to 20°.
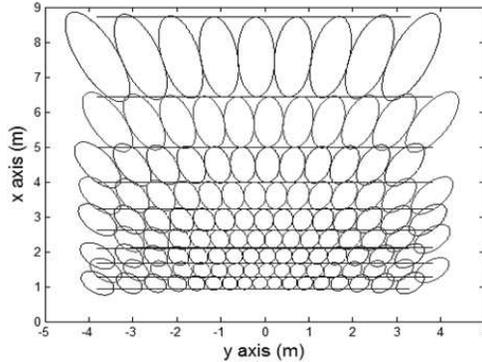
Figure 3. Linear scanning: antenna footprints plotted in an image sensed by a microwave radiometer with $\beta = 6°$ and based at $h = 3\,\text{m}$. The width of the image is fixed around $8\,\text{m}$. The incidence angle ψ, when the beam centerline points in direction parallel to x axis, ranges from $68°$ to $20°$.

It is evident that the advantage to observe the scene with the same incidence angle ψ at each sweep is achieved in spite of the production of an image of irregular shape.

2.2. Linear Scanning

In order to construct an image of rectangular shape, a linear scanning mode is required. For this purpose, the incidence angle ψ changes during a single sweep. Also, the sweeping angle γ_{sw} has to be varied accordingly to the width of the desired image. An example of linear imaging is shown in Fig. 3, simulating a radiometer again with $\beta = 6°$ and based at $h = 3\,\text{m}$. The incidence angle ψ, when the beam centerline points in direction parallel to x axis, ranges from $68°$ to $20°$. It is evident that the advantage to observe a scene with a rectangular shape is achieved in spite of the variation of the incidence angle ψ and of the footprint area at each sweep. Also, a superimposition of the boundary footprints is noticeable increasing the image width.

3. SCENE MODEL AND RESULTS

3.1. Soil without Fire

To compute the brightness temperature T_{B0} sensed by a scanning microwave radiometer based at height h, we have first considered an open space with an homogeneous soil without a fire. The observed T_{B0}

is given by [5]:

$$T_{B0} = T_s e_s + (1 - e_s)\left(T_{DN} + T_{BGD}e^{-\tau_\infty}\right) \qquad (2)$$

where e_s and T_s are the emissivity and the physical temperature of the soil respectively, T_{DN} is the downward atmospheric emission, T_{BGD} is the cosmic background (2.73 K) and τ_∞ is the atmospheric opacity. Since the radiometer is placed at an height of few meters, the upward atmospheric emission and the related optical depth have been neglected in (2). The computations of the radiometric temperatures were performed at 12.65 GHz, the operative frequency of the radiometer prototype developed in [5, 6].

With the aim to simulate T_{B0} in (2), we have modeled e_s as a function of incidence angle and polarization with the classical approach described in [8]. Then we have computed T_{DN} and τ_∞ at 12.65 GHz using a radiative transfer model [11] applied to a year of radiosoundings, extracting mean values as a function of the incidence angle taking benefit of the low variability of the downward atmospheric emission at this frequency. At different incidence angles, T_{DN} ranges from about 5–15 K and τ_∞ is usually less than 0.1 dB.

In the following simulated images produced in liner scanning mode, ensuring a regular shape (rectangular) of the investigated area, will be shown.

Figures 4 and 5 show an example of image of antenna temperature T_A for a scenario sensed in a linear scanning mode by the microwave
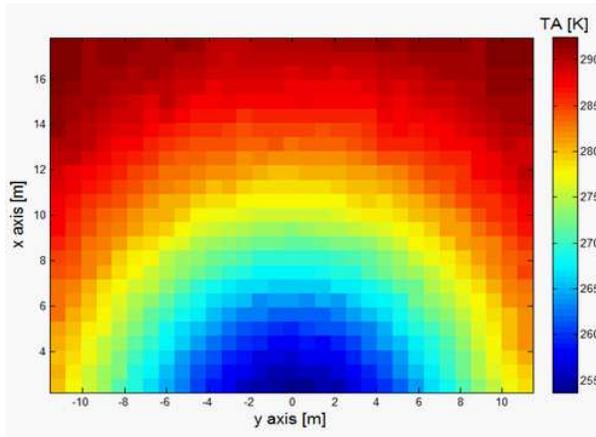

Figure 4. Image of antenna temperature T_A for vertical (V) polarization for a scenario (without fire) sensed in a linear scanning mode by the microwave radiometer based at $h = 10$ m, with $\beta = 6°$. The incidence angle ψ ranges from 60° to 14°.
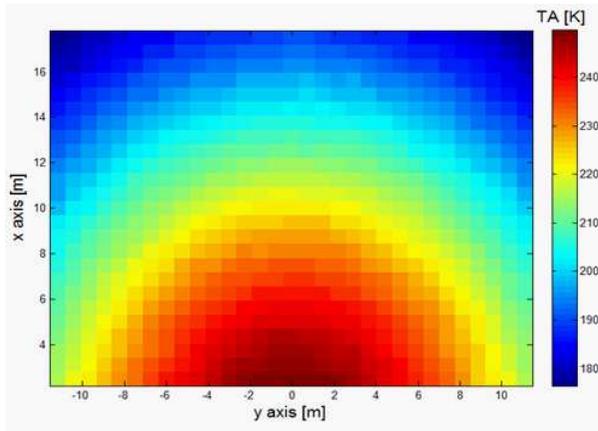
Figure 5. Image of antenna temperature T_A for horizontal (H) polarization for a scenario (without fire) sensed in a linear scanning mode by the microwave radiometer based at $h = 10\,\mathrm{m}$, with $\beta = 6°$. The incidence angle ψ ranges from 60° to 14°.

radiometer based at $h = 10\,\mathrm{m}$, for vertical (V) and horizontal (H) polarization respectively. Here after, the antenna power pattern $F(\theta, \varphi)$ is approximated with the fundamental Gaussian mode as detailed in [5, 12]. In the image scansion, $F(\theta, \varphi)$ is computed for each antenna beam direction (or antenna boresight), i.e., for all incident angles of each sweep. Since $F(\theta, \varphi)$ is provided for any (θ, φ) at the current beam position, the $(\theta, \varphi) \leftrightarrow (x, y)$ relationship is derived in order to estimate the antenna gain at each point (x, y) of the ground relative to the antenna boresight at each pointing.

In these simulations, $T_s = 293\,\mathrm{K}$ and the soil dielectric constant $(\varepsilon_r = 5 - j \cdot 0.01)$, employed for the computation of e_s, has been taken from [8] considering the range 10–18 GHz.

A zero-mean Gaussian random error was added to the map generations, with standard deviation of 0.4 K to simulate the instrumental noise. For a typical radiometer, the radiometric resolution usually ranges around 0.25–0.5 K.

To greatly improve the image resolution and to avoid gaps during the scans, a proper regular sampling step was selected, with partial overlapping of footprints not considered in the previous Fig. 3, especially for higher incidence angles. Also, it is assumed that the integration time of the radiometer is equal to the sampling time. For instance, operatively, with a sampling time of 0.5 sec., such an image should be created in about 7 minutes with a mechanical scanning. A trade-off among image resolution (pixel number), image production

time, radiometer integration time and scanning mechanism will be considered for each prospective actual campaign.

The brightness temperature variation obtained in the simulation results is due to the antenna polarization (compare both Fig. 4 vs Fig. 5) and to the incidence angle. In particular, the impact of the incidence angle is less pronounced observing the soil in vertical polarization. In this case, the apparent soil temperature variation is about 35 K (more than 60 K in horizontal polarization).

3.2. Soil with Fire

With the aim to simulate the brightness temperature T_{BF} again in an open space with an homogeneous soil but in presence of fire, the relation becomes [5]:

$$T_{BF} = \left[T_F e_F + (1 - e_F) \left(T_{DN} + T_{BGD} e^{-\tau \infty} \right) \right] q + T_{B0} (1 - q) \quad (3)$$

where e_F and T_F are the emissivity and the average physical temperature of the fire respectively. The parameter q, as quantitatively explained in [5], is the filling factor, defined as the power received from a fire source relative to that which would be received from a source having the same brightness but extending over the whole antenna pattern.

So, artificial target scenes have been constructed and a radiometric imaging simulated, recording the samples of a scanning radiometer. In such scenes, fires of different size and position were considered, with $e_F = 0.9$ [5] and T_F up to 1000 K.

Figures 6 and 7 show an example of T_A image, for both V and H polarization, for the scenario and geometry analyzed in Figs. 4 and 5. In these figures, an example of unfavourable case, such as a fire of little dimension $(0.5 \times 0.5 \, \text{m})$ in the early stage $(700 \, \text{K})$, is presented. The fire spot is positioned in the upper and lower side of the scene for V and H polarization respectively.

These simulations assess the fire identification capability for little fires, with a better recognition in the lower side where the broadening of the footprint is inferior.

However, a bare soil with a fire is an operative scenario where visible and IR sensors are greatly useful and performing with respect to a microwave imager. On the contrary, visible and IR sensors fail in the presence of a vegetation canopy optically masking the fire source and the smoke plume in the early stage.

3.3. Soil Covered by Vegetation in the Presence of Fire

The simulation of the brightness temperature T_{BFV} for an open space with an homogeneous soil covered by a vegetation layer, in presence of fire, obeys the following relation:

$$T_{BFV} = T_{FV} + T_{SV} + T_{BV} + T_{VrS} + T_{VrF} + T_{skyr} \qquad (4)$$

where:

- $T_{FV} = e_F T_F t_V q$, emission of the fire attenuated by the overlaying vegetation canopy with transmissivity t_V.
- $T_{SV} = e_S T_S t_V (1 - q)$, emission of the bare soil attenuated by the vegetation, where $(1 - q)$ describes the fraction of the footprint not covered by the fire.
- $T_{BV} = e_V T_V$, direct emission of the vegetation layer, where T_V is the physical temperature of the vegetation and e_V its emissivity.
- $T_{VrS} = (1 - e_S) T_{BV} t_V (1 - q)$, downward emission of the vegetation reflected by the soil and attenuated by the vegetation layer.
- $T_{VrF} = (1 - e_F) T_{BV} t_V q$, downward emission of the vegetation reflected by the fire and attenuated by the vegetation layer.
- $T_{skyr} = r_V (T_{DN} + T_{BGD} e^{-\tau \infty})$, downward brightness temperature emitted by the sky and reflected by the vegetation, with r_V the vegetation reflectivity.
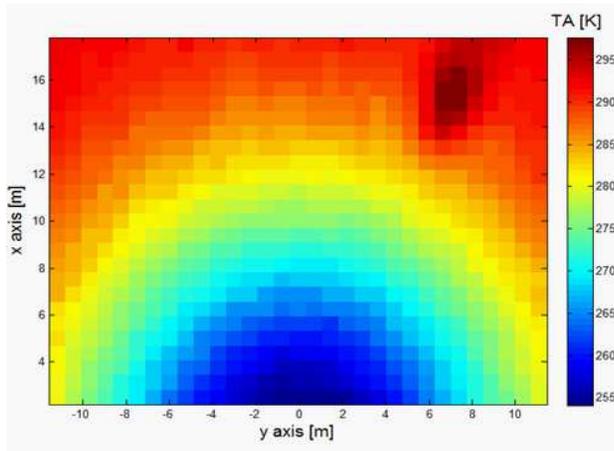

Figure 6. Image of antenna temperature T_A for V polarization for a scenario sensed in a linear scanning mode by the microwave radiometer based at $h = 10$ m, with $\beta = 6°$. The incidence angle ψ ranges from $60°$ to $14°$. The fire (0.5×0.5 m, 700 K) is placed in the upper-right side of the scene.
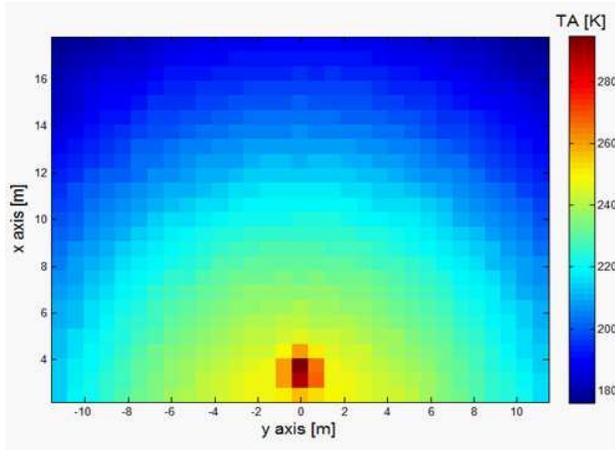
Figure 7. Image of antenna temperature T_A for H polarization for a scenario sensed in a linear scanning mode by the microwave radiometer based at $h = 10\,\mathrm{m}$, with $\beta = 6°$. The incidence angle ψ ranges from $60°$ to $14°$. The fire $(0.5 \times 0.5\,\mathrm{m}, 700\,\mathrm{K})$ is placed in the lower-middle side of the scene.

Again, since the radiometer is placed at an height of few meters, the upward atmospheric emission and the related optical depth, due to the atmospheric layer between the top of vegetation and the sensor at height h, have been neglected in (4).

Therefore, the brightness temperature T_{BFV} in the observation direction is due to the sum of many different contributions, the most important of them being the direct emission of the fire and soil attenuated through the vegetation layer, and the direct contribution of the vegetation. Emission and attenuation from the vegetation depend on parameters like total plant water content and shape and dimension of the vegetation components.

Typical forest canopy emissivity (e_V) assumes high values, up to 0.95, and differences with incidence angle and polarization are negligible [8, 13]. Concerning the forest transmissivity t_V, it depends on complexity of the canopy geometry and on size and density of the leaves, branches and trunks relative to the wavelength. Limited studies and experiments are available in literature and for the simulation purposes we have considered two empirical models: the first, proposed by Matzler [14], hereafter named Model_1, and the second by [15], hereafter named Model_2.

Model_1, for typical dense beech forests, computed at $12.65\,\mathrm{GHz}$, provides a $t_V = 0.28$ during winter days, while during warmer days it decreases under $t_V = 0.06$ with increasing incidence angles. In the

following, we will consider the model for warmer days.

Model_2, derived from actual ground-based radiometric measurements (19–37 GHz) for forests of black spruce, birch, aspen and jack pine, provides a relation between t_V and forest stem volumes. Forest transmissivity t_V settles at values around 0.3–0.4 for high incidence angles and higher stem volumes.

As stated in [14, 15], the forest reflectivity r_V is negligible and T_V is close to T_s. Also, the estimated t_V values were similar for both polarizations. Since forest transmissivity decrease with frequency, the selected 12.65 GHz operation frequency is a good trade-off between penetration capability and reasonable antenna size.

Model_1 and Model_2 can be assumed as limits for unfavorable and favorable cases of dense forest transmissivity, respectively.

3.4. Results

To better understand the identification capability of the fire by the ground-based microwave radiometer in the presence of vegetation canopy, the computation of the radiometric contrast (RC) is more performing. The radiometric contrast is the antenna temperature difference in the presence of fire with respect to the standard background, i.e., in the absence of fire. Operatively, the RC has to be computed, continuously, for two consecutive images in time.

Hereafter, we will consider simulations with $h = 10$ m, as a trade-off between a reasonable placement of a radiometer (for instance on a tower or a pole) and its footprint broadening on the ground.

Figures 8 and 9 show an example of RC image for T_A, for both polarizations, with $\beta = 6°$, for the same scenario and fire characteristics of Figs. 6 and 7, respectively. In these simulations, we refer to Model_2 for forest transmissivity ($t_V = 0.3$), with $e_V = 0.7$ and $T_V = 292.8$ K. When we will refer to Model_1, $e_V = 0.85$ and $T_V = 292.8$ K will be applied. It is worth to note that once fixed t_V, perturbing e_V up to a maximum of 0.15, the RC fluctuations are generally below 1 K.

Again, a zero-mean Gaussian random error with standard deviation of 0.4 K was added to simulate measurement errors.

In Table 1, RC values detected in different situations, with a fire of little dimension in the early stage (0.5×0.5 m, 700 K), are reported. We have considered both forest transmissivity models, antenna half-power beam width $\beta = 6°$ and $\beta = 3°$, and fire position again in the upper-right side and in the lower-middle side of the scene, referred as unfavorable and favorable cases, respectively. In Table 2, the same but with a fire of 1×1 m.

The maximum RC, i.e., when the filling factor is maximum, is very weakly influenced by the polarization.
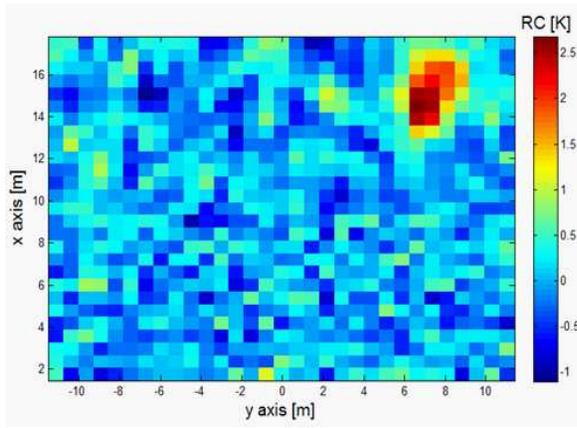
Figure 8. Image of radiometric contrast (RC), K, for V polarization for a scenario sensed in a linear scanning mode by the microwave radiometer based at $h = 10\,\text{m}$, with $\beta = 6°$. The incidence angle ψ ranges from $60°$ to $14°$. The fire $(0.5 \times 0.5\,\text{m}, 700\,\text{K})$ is placed in the upper-right side of the scene, with forest transmissivity referred to Model_2.
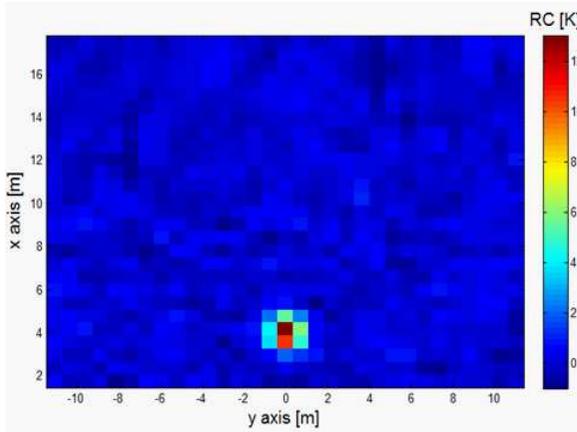

Figure 9. Image of antenna temperature T_A for H polarization for a scenario sensed in a linear scanning mode by the microwave radiometer based at $h = 10\,\text{m}$, with $\beta = 6°$. The incidence angle ψ ranges from $60°$ to $14°$. The fire $(0.5 \times 0.5\,\text{m}, 700\,\text{K})$ is placed in the lower-middle side of the scene, with forest transmissivity referred to Model_2.

With a fire of $0.5 \times 0.5\,\text{m}$ and a very low forest transmissivity (Model_1), the radiometric contrast throughout the image is low, even below the noise level, and the fire detection is not possible, both for

Table 1. Radiometric contrast (RC) for T_A for a fire of little dimension in the early stage (0.5×0.5 m, 700 K).

β	Fire position (y, x) [m]	Model t_V	Max RC [K] pol H	Max RC [K] pol V
3°	0, 4	Model_1	5.9	6.2
3°	7, 15	Model_1	0.8	1.0
6°	0, 4	Model_1	2.4	2.3
6°	7, 15	Model_1	0.5	0.3
3°	0, 4	Model_2	32.9	32.1
3°	7, 15	Model_2	8.8	8.3
6°	0, 4	Model_2	13.4	13.3
6°	7, 15	Model_2	2.7	2.7

Table 2. Radiometric contrast (RC) for T_A for a fire of little dimension in the early stage (1×1 m, 700 K).

β	Fire position (y, x) [m]	Model t_V	Max RC [K] pol H	Max RC [K] pol V
3°	0, 4	Model_1	15.5	15.4
3°	7, 15	Model_1	3.7	3.1
6°	0, 4	Model_1	8.2	8.4
6°	7, 15	Model_1	1.8	1.4
3°	0, 4	Model_2	86.2	85.8
3°	7, 15	Model_2	33.3	30.9
6°	0, 4	Model_2	45.9	45.2
6°	7, 15	Model_2	11.1	10.7

$\beta = 6°$ and $\beta = 3°$. Moreover, very few Kelvin of RC could occur with different solar illumination and irradiation of the upper layers of the scenario or with other natural phenomena during two consecutive images. Finally, as Fig. 8 also suggests, a threshold of 2 or 3 K can be assumed as limit for false alarms.

But, in the same conditions with $\beta = 3°$, increasing the fire dimension (1×1 m), the maximum RC proves the possibility of

detection of a fire in the early stage under a very dense forest. With a forest canopy modelled with $t_V = 0.3$, the fire detection seems to be possible even with $\beta = 6°$ and fire dimension of 0.5×0.5 m, taking also into account the broadening of the antenna footprint with increasing incidence angles.

With $\beta = 3°$, Model_2 and fire dimension of 0.5×0.5 m, the fire detection is still possible with a radiometer based at $h = 15$ m (max RC ranges from around 3 K to 14 K throughout the image for both polarizations).

Finally, considering different values of forest transmissivity, these little fires can be safely detected if t_V is greater than 0.1.

Concerning the maximum size of a possible scanned area, with $\beta = 3°$, Model_2 and fire dimension of 1×1 m, to avoid false alarms (i.e., to ensure RC greater than 3 K), an image of about 80×70 m can be sensed.

4. CONCLUSION

The simulated imaging of a ground-based microwave radiometer under different environmental and operative conditions seems to be promising for fire spot detection. Moreover, it is useful especially when visible and IR sensors fail, such as in the presence of dense vegetation optically masking the fire source and the smoke plume.

With regard to forest areas, the proposed simulations have the aim to establish performances and limits in the identification capability of little fires by means of microwave radiometry. It has been seen that the radiometric contrast can be computed as the difference between two successive scans of the same area. If a 3 K threshold is used on the radiometric contrast, fires of dimensions around 1 square meters can safely be detected under the vegetation at a distance of about 80 m.

Also, taking advantage of the low-cost radiometer considered in the framework of this work [5, 6], a network of radiometers can be considered to increase the monitored area [16]. Otherwise, it can be mounted aboard an unmanned aircraft vehicle (UAV) [17, 18], although a permanent scan is not possible due to the maximum duration of each mission.

Further application scenarios suitable for the microwave fire detection could be: i) large storage areas of solid fuels like coal, wood pellets, woodchips, used tires and the like; ii) waste bunkers; iii) large transportation infrastructures, aircraft hangars, railway freight deposits, container terminals; iv) high rack storage areas; v) large industrial plants e.g., (petro-) chemical industry, wood processing plants. In all these cases a network of radiometers will have the

advantage to continuously monitor a large area, even if to improve the image resolution more time is needed to create the image itself.

REFERENCES

1. Ayanz, M., N. Ravail, V. Kelha, and A. Ollero, "Active fire detection for fire emergency management: Potential and limitations for the operational use of remote sensing," *Nat. Hazards*, Vol. 35, No. 3, 361–376, 2005.

2. Coppo, P., S. Fini, G. Luzi, T. Mazzoni, P. Ferrazzoli, L. Guerriero, and G. Lio, "Microwave radiometry applied to forest fires: Operational aspects and model analysis," *Proc. of the 11th EARSeL Symposium*, 259–265, Graz, 1991.

3. Kaiser, T., T. Kempka, and K. Solbach, "Microwaves in fire detection," *Fire Safety Journal*, Vol. 41, No. 6, 327–333, 2006.

4. Luzi, G., P. Coppo, P. Ferrazzoli, S. Gagliani, and T. Mazzoni, "Microwave radiometry as a tool for forest fire detection: Model analysis and preliminary experiments," *Microwave Radiometry and Remote Sensing of the Earth's Surface and Atmosphere*, 411–418, D. Solimini, Ed., VSP Press, Utrecht, The Netherlands, 1995.

5. Tasselli, G., F. Alimenti, S. Bonafoni, P. Basili, and L. Roselli, "Fire detection by microwave radiometric sensors: Modelling a scenario in the presence of obstacles," *IEEE Trans. Geosci. Remote Sens.*, Vol. 48, No. 1, 314–324, 2010.

6. Alimenti, F., S. Bonafoni, S. Leone, G. Tasselli, P. Basili, L. Roselli, and K. Solbach, "A low-cost microwave radiometer for the detection of fire in forest environments," *IEEE Trans. Geosci. Remote Sens.*, Vol. 46, No. 9, 2632–2643, 2008.

7. Luthi, T. and C. Matzler, "Stereoscopic passive millimeter-wave imaging and ranging," *IEEE Trans. Microw. Theory Tech.*, Vol. 53, No. 8, 2594–2599, 2005.

8. Ulaby, F. T., R. K. Moore, and A. K. Fung, *Microwave Remote Sensing: Active and Passive*, Artech House, 1981.

9. Kemppinen, M. U., "Airborne imaging radiometer scan simulation," *IEEE Trans. Geosci. Remote Sens.*, Vol. 33, No. 3, 660–669, 1995.

10. Kemppinen, M. U. and M. T. Hallikainen, "The theory and mechanical realization of an ideal scanning method for a single-channel imaging microwave radiometer," *IEEE Trans. Geosci. Remote Sens.*, Vol. 30, No. 4, 743–749, 1992.

11. Schroeder, J. A. and E. R. Westwater, "Users' guide to WPL microwave radiative transfer software," NOAA Tech. Rpt. ERL-

219 WPL-213, 84, NOAA/Environmental Research Laboratories, Boulder, CO, 1991.

12. Goldsmith, P. F., *Quasioptical Systems: Gaussian Beam, Quasioptical Propagation and Applications*, IEEE Press, Piscataway, NJ, 1998.

13. Karbou, F., C. Prigent, L. Eymard, and J. Pardo, "Microwave land emissivity calculation using AMSU measurements," *IEEE Trans. Geosci. Remote Sens.*, Vol. 43, No. 5, 948–959, 2005.

14. Matzler, C., "Microwave transmissivity of a forest canopy: Experiments made with a beech," *Remote Sens. Environ.*, Vol. 48, No. 2, 172–180, 1994.

15. Pardé, M., K. Goita, A. Royer, and F. Vachon, "Boreal forest transmissivity in the microwave domain using ground based measurements," *IEEE Geosci. Remote Sens. Lett.*, Vol. 2, No. 2, 169–171, 2005.

16. Viani, F., L. Lizzi, M. Donelli, D. Pregnolato, G. Oliveri, and A. Massa, "Exploitation of parasitic smart antennas in wireless sensor networks," *Journal of Electromagnetic Waves and Applications*, Vol. 24, No. 7, 993–1003, 2010.

17. Sharawi, M. S., O. A. Rawashdeh, and D. N. Aloi, "2.4 GHz printed antennas embedded in small UAV wing structures," *Journal of Electromagnetic Waves and Applications*, Vol. 24, No. 4, 463–474, 2010.

18. Sharawi, M. S., "Dual element monopole antennas embedded in small UAV wing structures with beam-steering capability," *Journal of Electromagnetic Waves and Applications*, Vol. 24, No. 11–12, 1633–1645, 2010.